Green Chemistry

A Simple Method for Producing Bio-Based Anode Materials for Lithium-Ion Batteries

Journal:	*Green Chemistry*
Manuscript ID	GC-ART-07-2020-002286.R1
Article Type:	Paper
Date Submitted by the Author:	09-Sep-2020
Complete List of Authors:	Sagues, William; North Carolina State University, Forest Biomaterials; National Renewable Energy Laboratory Yang, Junghoon; National Renewable Energy Laboratory Monroe, Nicholas; North Carolina State University, Forest Biomaterials Han, Sang-Don; National Renewable Energy Laboratory, Chemistry & Nanoscience Center Vinzant, Todd; National Renewable Energy Laboratory, Yung, Matthew; National Renewable Energy Laboraory, Jameel, Hasan; NC State University, Forest Biomaterials Nimlos, Mark; National Renewable Energy Laboratory, Park, Sunkyu; North Carolina State University, Forest Biomaterials

A Simple Method for Producing Bio-Based Anode Materials for Lithium-Ion Batteries

William J. Sagues,[a,b,c] Junghoon Yang,[d] Nicholas Monroe,[a] Sang-Don Han,[d] Todd Vinzant,[c] Matthew Yung,[c] Hasan Jameel,[a] Mark Nimlos,[c] & Sunkyu Park[a*]

Author Information:

[a]Department of Forest Biomaterials, North Carolina State University, 2820 Faucette Dr., Raleigh, NC 27695, USA

[b]Department of Biological & Agricultural Engineering, North Carolina State University, 3110 Faucette Dr., Raleigh, NC 27695, USA

[c]National Renewable Energy Laboratory, FTLB Lab, 16253 Denver West Parkway, Golden, CO 80401, USA

[d]Materials and Chemical Science and Technology Directorate, National Renewable Energy Laboratory, 15013 Denver West Parkway, Golden, CO 80401, USA

Correspondence and requests for materials should be addressed to Sunkyu Park: sunkyu_park@ncsu.edu

Abstract

A simple and scalable method for producing graphite anode material for lithium-ion batteries is developed and demonstrated. A low-cost, earth abundant iron powder is used to catalyze the conversion of softwood, hardwood, cellulose, glucose, organosolv lignin, and hydrolysis lignin biomaterials to crystalline graphite at relatively low temperatures (< 1200°C). Biographite materials are characterized and compared based on graphite mass yield, graphite crystallite size, degree of graphitization, graphite uniformity, iron catalyst distribution, and graphite morphology.

Particle size, heating method, and intermediate liquid phase formation, among other factors, play important roles in the graphitization process. Molten eutectic iron carbides solubilize disordered carbon and precipitate graphite platelets of crystallite size comparable to commercial graphite. Softwood-derived biographite is of the highest quality and demonstrates excellent electrochemical performance as anode material in a lithium-ion coin cell with 89% capacity retention over 100 cycles and > 99% Coulombic efficiency.

Introduction

Graphite is a crystalline allotrope of carbon consisting of sp2 bonded carbon atoms densely arranged in parallel-stacked layers.[1] Graphite has a high melting temperature (3900°C) and is relatively chemically inert, making it suitable for harsh industrial applications that utilize high temperatures and/or corrosive chemicals, such as refractories and electrodes in metals processing and neutron moderators in nuclear fission reactors.[1] In addition, graphite's high electrical conductivity and ability to intercalate particular ions make it ideal for use in electrochemical applications, such as lithium-ion batteries, supercapacitors, and fuel cells.[1,2] The highest demand for graphite currently comes from metals processing, however, growth in the manufacturing of lithium-ion cells for electric vehicles and stationary energy storage is rapidly increasing the demand for battery-grade graphite.[2–7] The anode of a lithium-ion cell is predominantly made of graphite, constituting 15 - 30% of the total cell mass and 11 - 23% of total cell manufacturing cost ($10 - $20 per kilogram).[8,9] The British Geological Survey lists graphite as a top supply risk material, and the United States Geological Survey classifies graphite as a strategic and critical mineral.[10,11] There are two broad classifications of graphite for commercial use: natural and synthetic. Battery-grade graphite used in lithium-ion anodes is typically a mixture of synthetic and natural graphite.[2,8,12] Natural graphite is mined from

geographically constrained natural deposits and subsequently purified using a series of energy- and chemical-intensive processes.[1,2,13,14] Battery-grade natural graphite is typically milled and shaped into spherical form prior to purification.[12] Purification of battery-grade natural graphite typically involves intensive use of hydrofluoric acid, which is toxic and damaging to public health and the environment.[2,9,14] Natural graphite concentrates are typically 90 – 98% carbon, with the remainder consisting of a mix of inorganic impurities, including carbonate and silicate minerals.[14] Hydrofluoric acid is typically used to remove the silicate impurities from the graphite concentrate. Thus, alternative methods of purification that avoid the use of hydrofluoric acid would lessen societal and environmental impacts. Synthetic graphite is typically produced by processing low-sulfur petroleum distillation residues via delayed coking at ~1500°C to form needle coke, which is then graphitized at 2500 – 3000°C for over a week.[8,15] Heavy petroleum distillation residues with aromatic carbon contents above 60% and sulfur contents less than 1% are suitable graphite precursors.[1,15] Delayed coking and coke calcining form needle coke, which consists of turbostratic crystallites with no evidence of long-range three dimensional order.[1,16] During graphitization, crystallites form and grow in size (Lc) greater than 20 nm and the interlayer spacing (d) of the graphitic sheets decreases from ~0.344 nm to a minimum of 0.335 nm.[1]

Lithium-ion battery manufacturers are trending towards higher percentages of synthetic graphite in their anode materials, with 70% of anode material expected to be synthetic graphite in 2030.[9] Compared to natural graphite, synthetic graphite has better performance and reliability. However, synthetic graphite has a multitude of flaws, including its use of geographically constrained sulfur-containing petroleum residues as feedstock, slow rate of production, intensive use of fossil energy and the resultant CO_2 emissions in production (7.5 – 9.9 kg CO_2/kWh), and

high cost ($10 - $20/kg).[8,9,17] Thus, the energy storage industry would greatly benefit from innovative technologies that convert domestic, low-cost, sustainable, and non-toxic carbonaceous materials into high quality, low-cost graphite anodes at relatively low temperatures and without the use of hydrofluoric acid.

Most carbonaceous materials treated at high temperatures (> 2000°C) under inert atmospheres and without catalysts will carbonize to form disordered, amorphous carbon materials with cross-linked domains or ordered soft carbon materials with graphitic domains.[1] As early as 1951, glucose, cellulose, lignocellulosic biomass, and related biomaterials were proven to be non-graphitizing materials that form disordered, amorphous char when treated at high temperatures.[1,18,19] Amorphous, bio-based carbon materials of high surface area have the potential for high specific capacity anodes in lithium- and sodium-ion batteries, and work is ongoing to overcome challenges including electrode thickness, irreversible capacity loss, and cycling stability.[20–22] In the near-term, commercial lithium-ion batteries will continue to rely on highly graphitic material for anodes.[9] Although some carbonized biomaterials show evidence of graphitic structure, the crystallites are typically small and heavily diluted in disordered carbon, thus making them not suitable for near-term lithium-ion anode applications.[18,23,24] The abundance of oxygen, lack of intermediate mesophase during carbonization, and lack of polyaromatic hydrocarbons make biomaterials generally non-graphitizing.[1,15,18] Notably, multiple high-impact published studies have recently demonstrated catalytic conversion of lignocellulosic biomass and other biomaterials to battery-grade biographite at relatively low temperatures (1000 - 2000°C).[25–30] The term “biographite” refers to graphite derived from biogenic carbon. Banek et al. (2018) converted multiple lignocellulosic feedstocks to high quality biographite via a 2 step process: 1) carbonization at 600°C for 30-min to form biochar and 2) graphitization of thin composites of

biochar mixed with iron powder using a high intensity laser.[26] The use of laser ablation and thin carbon/iron substrates were proven critical to the graphitization process due to the high surface temperatures achieved (1500 – 2000°C) by the laser and inability of the laser's radiative energy to penetrate deep into solid materials. The biographite produced was of high quality and performed well in lithium-ion cells, however, the method of graphitization is difficult to scale due to the necessity of a high intensity laser and thin substrates. Zhao et al. (2018) converted glucose to battery-grade biographite via a different 2 step process: 1) carbonization at 1100°C for 3h to form biochar and 2) graphitization of a mixture of biochar and magnesium at 800 - 1000°C for 3 - 20h using a tube furnace.[29] The biographite produced was of high quality and performed well in a lithium-ion cell, however, no lignocellulosic feedstocks were included in the study. Gomez-Martin (2018) converted medium-density fiberboard (MDF) to battery-grade biographite by impregnating iron chloride into the MDF via soaking in an aqueous solution prior to treatment at 850 - 2000°C in a tube furnace. The biographite produced at 2000°C was of high quality and performed reasonably well in a lithium-ion cell, however, soaking in iron chloride solution and treatment at such a high temperature decrease process viability.[27] Thompson et al. (2015) converted softwood sawdust to partially graphitized material by impregnating iron nitrate into the sawdust via soaking in an aqueous solution prior to treatment at 800°C in a tube furnace.[28] The partially graphitized material was not tested in lithium-ion cells, because the quality of the biographite was not ideal and the performance would have been subpar.

Biomaterials vary significantly in their composition, and there is a lack of knowledge regarding how various components and building blocks, including glucose, cellulose, and lignin, affect graphitization. Previous research has demonstrated the inability of various lignins to graphitize in the production of carbon fibers.[24] Carbon fibers made from Rayon, a derivative of

cellulose, tend to be more graphitic than lignin-based carbon fibers.[1] Thus, cellulose appears to be more susceptible to graphitization than lignin, but there hasn't been a study on whether this observation holds true in the case of catalytic graphitization at relatively low temperatures (< 1200°C). Also, there hasn't been a study to determine whether the relatively complex cellular structures of hardwoods inhibit catalyst transport and provide biographite of lesser quality than softwoods.[31] Notably, there has yet to be a study published in which a multitude of biomaterials of varying compositions and particle sizes are catalytically graphitized using a simplistic, dry mix, single-step process in a traditional tube furnace at relatively low temperatures (< 1200°C). Herein, we demonstrate such a simplistic method of catalytic graphitization to convert a multitude of biomaterials to high quality biographite. To the best of our knowledge, there has been no published study in which a similar method of such simplicity has been used to catalytically convert biomaterials to high quality biographite.

Experimental

Materials

The commercial synthetic graphite used as the primary reference for characterization is from Asbury Carbons.[32] Several other graphite materials from the literature are used as references for electrochemical performance.[33–36] The softwood biomaterial is clean (no bark) loblolly pine from the southeastern US and two particle sizes are used: 150 – 425um (baseline) and 710 – 1000um. The hardwood biomaterial is a mixture of hardwood obtained from the southeastern US and two particle sizes are used: 150 – 425um (baseline) and 710 – 1000um. The cellulose biomaterial is softwood market pulp from the southeastern US and one particle size is used: < 500um. The glucose and organosolv lignin biomaterials are obtained from Sigma Aldrich and one particle size is used for both: < 500um. The hydrolysis lignin is obtained from NCSU

after autohydrolysis and enzymatic digestion of hardwood and one particle size is used: < 500um. The Kraft lignin is a softwood Kraft lignin obtained from a pulp mill in the southeastern US (size < 500um). The iron catalyst is an iron powder of spherical particle size < 10um and is obtained from Sigma Aldrich. The hydrochloric acid is of 37 wt% and is obtained from Fisher Scientific.

Catalytic Graphitization & Acid Washing

The baseline method of graphitization involves mixing dry biomaterial with iron powder catalyst (30 wt%) prior to graphitization in a tube furnace under nitrogen (1L/min). The "baseline" heating ramp is as follows: furnace on, 25 – 600°C at 3°C/min, 600 – 1200°C at 10°C/min, furnace off, natural cool down. The "fast" heat ramp is as follows: furnace on, 25 – 1200°C at 10°C/min, furnace off, natural cool down. The "hold" heat ramp is as follows: furnace on, 25 – 600°C at 3°C/min, 600 – 1200°C at 10°C/min, hold at 1200°C for 60 minutes, furnace off, natural cool down. The iron catalyst is removed from the biographite via reaction with hydrochloric acid. The reflux is carried out in excess by lightly boiling a 5 wt% loading of biographite + iron in concentrated hydrochloric acid (37 wt%) for three hours. The purified graphite is separated via filtration and dried. The state-of-the-art methods of purifying graphite for battery anode applications typically involve the use of hydrofluoric acid, and thus our method of using hydrochloric acid helps to lessen environmental and environmental impacts.

X-ray Diffraction

X-ray diffraction patterns of powdered samples are taken on a Rigaku Ultima IV X-ray diffractometer equipped with a copper X-ray source, K-beta filter, and dTex detector. Diffraction patterns are obtained using a data spacing of 0.02 degrees at a scan rate of

2.5° two-theta/minute. PDXL integrated X-ray powder diffraction software is used to estimate graphite crystal size based on the Scherrer Equation.

Raman Spectroscopy

Laser Raman spectra are obtained on powdered samples at room temperature using a Horiba Jobin-Yvon LabRam HR800 spectrometer with a 50x microscope objective microprobe in the back scattering geometry and a 532 nm Nd:YAG frequency-doubled laser (Torus). Raman spectra mapping (5-point) is conducted to ensure representative estimates of degrees of graphitization.

Scanning Electron Microscopy & Energy Dispersive X-ray Spectroscopy

Dry biographite samples with and without iron are used without further preparation for SEM. Samples are placed on aluminum stubs using two-sided carbon tape. The samples do not require coating due to the high electrical conductivity of the graphitic carbon. Imaging is performed using a FEI Quanta 400 FEG SEM instrument operating under vacuum (0.45 Torr) at a beam accelerating voltage of 20 keV and capturing secondary electrons with an Everhart-Thornley detector. The FEI Quanta 400 FEG SEM is coupled with an energy dispersive x-ray detector to obtain spectral maps that are interpreted via TEAM software developed by EDAX.

Transmission Electron Microscopy

A Titan G2 Transmission Electron Microscope (TEM) instrument with accelerating voltage of 200kV is used to analyze samples. Samples are prepared by mixing a small volume of biographite powder with clean methanol, ultrasonicating the solution for 2 minutes, and depositing a small aliquot onto an ultrathin carbon TEM support grid.

Brunauer-Emmett-Teller Surface Area

The Brunauer-Emmett-Teller (BET) surface area is determined using Micromeritics Instrument Corporation's Gemini VII 2390 instrument. A 0.15 - 0.20 g sample is loaded in the quartz tube and the sample is degassed at 220°C with nitrogen for 2h. Multipoint BET surface area is calculated from the linear relative pressure regime of $0.05 < P/P_0 < 0.30$. Total pore volume is calculated at $P/P_0 = 0.98$. Micropore volume is calculated by summation of pore volumes with diameter < 2nm.

Electrochemical Tests

Softwood-derived biographite electrodes are prepared from slurry with the following composition: active material (92 wt%); Super C45 (2 wt%), which is used as a conductive agent, and a binder (polyvinylidenedifluoride, 6 wt%), which is dissolved in N-methyl-2-pyrrolidone (NMP). This slurry is pasted onto Cu-foil current collector and dried at 120°C for 12 h under vacuum. Electrodes with a diameter of 14 mm are punched, and the average active material loading density is 3.5 mg cm^{-2}. The electrochemical performance of the prepared electrodes is evaluated using CR2032 coin-type cells assembled in an Ar-filled glove box. Li metal is used as a counter and reference electrode, and a solution of 1.2M $LiPF_6$ + EC:EMC (3:7 by wt.) (Gen II electrolyte) is employed as the electrolyte. Galvanostatic discharge/charge tests are performed in a range of 0.005 to 1.5 V (*vs* Li/Li^+, hereafter) at a variety C-rate (1 C corresponded to about 372 mAg^{-1}).

Results & Discussion

X-ray diffraction (XRD) and Raman spectroscopy are the two main methods used to qualify and quantify the graphite crystallinity of the biographite products. The 002 and 100 reflections of graphitic materials, which correspond to 2θ diffraction angles of 26.5° and 42.4°, allow for the quantification of graphitic crystallite size in the c-direction (Lc) and a-direction

(La), as shown in Figure S1. Crystallite size (L) is inversely proportional to the XRD peak intensity full-width at half-height (B), as shown in Equation S1, and thus tall and narrow peaks indicate larger graphite crystallites than short and wide peaks. Graphitic structure can also be characterized by measuring the Raman shifts from irradiating samples with light of particular wavelengths. Two primary Raman shifts are associated with graphitic materials: a small intensity shift at ~1350 cm^{-1} (*D* shift) and a large intensity shift at ~1575 cm^{-1} (*G* shift). The average graphite crystallite size (L) is inversely proportional to the ratio of D and G intensities (I_D/I_G), as shown in Equation S2. The degree of graphitization (α) can be estimated by using Equation S3.

The baseline method of catalytic graphitization is capable of converting a multitude of various biomaterials into high quality graphite, as shown in Figure 1. Kraft lignin is the only biomaterial incapable of graphitization, which appears to be partly due to the presence of sulfur and inadequate phase change of iron during thermal treatment. After a successful graphitization, the iron catalyst is of the allotropic form alpha, as shown in Figure 2A. Kraft lignin is the only biomaterial that contains iron catalyst of two allotropic forms after thermal treatment: alpha and gamma. In addition, Kraft lignin is the only biomaterial with an appreciable quantity of sulfur (1.3 wt%). As shown in Figure 2B, residual sulfur is detected in the biographite. Sulfur and iron are highly reactive, and thus their interaction likely reduces the efficacy of the catalyst.[37–39] However, sulfur reactivity cannot account for all iron catalyst inactivity and thus further research into the inherent limitations of Kraft lignin graphitization should be conducted. The condensed nature of Kraft lignin might result in high bond dissociation energies, and thus would require a higher temperature for graphitization. Future work on Kraft lignin should investigate treatment temperatures higher than 1200°C.

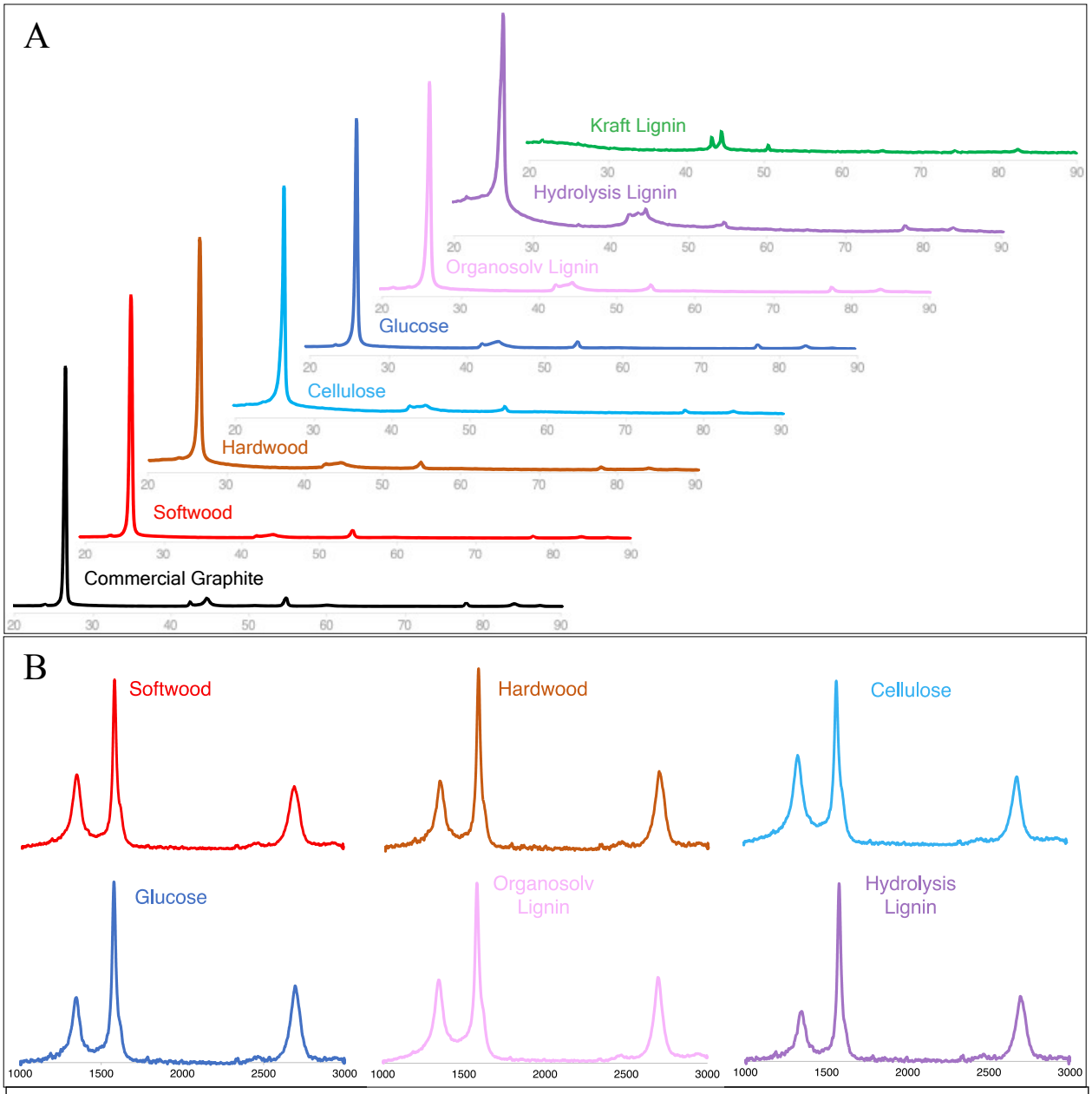

Figure 1. A) X-ray diffractograms with 2θ angles of diffraction listed on x-axis and B) Rama spectra with chemical shift listed on x-axis of biographite materials produced from the baseline method of iron-catalyzed graphitization. Biographite materials had iron removed prior to analysis. Commercial graphite refers to Asbury Carbons' synthetic graphite product and is included as a reference. Softwood refers to loblolly pine obtained from the southeastern US. Hardwood refers to mixed hardwood obtained from the southeastern US. Cellulose refers to softwood market pulp obtained from the southeastern US. Glucose and organosolv lignin obtained from Sigma Aldrich. Hydrolysis lignin refers to purified lignin after autohydrolysis and enzymatic digestion of hardwood. Kraft lignin refers to softwood Kraft lignin obtained from the southeastern US.

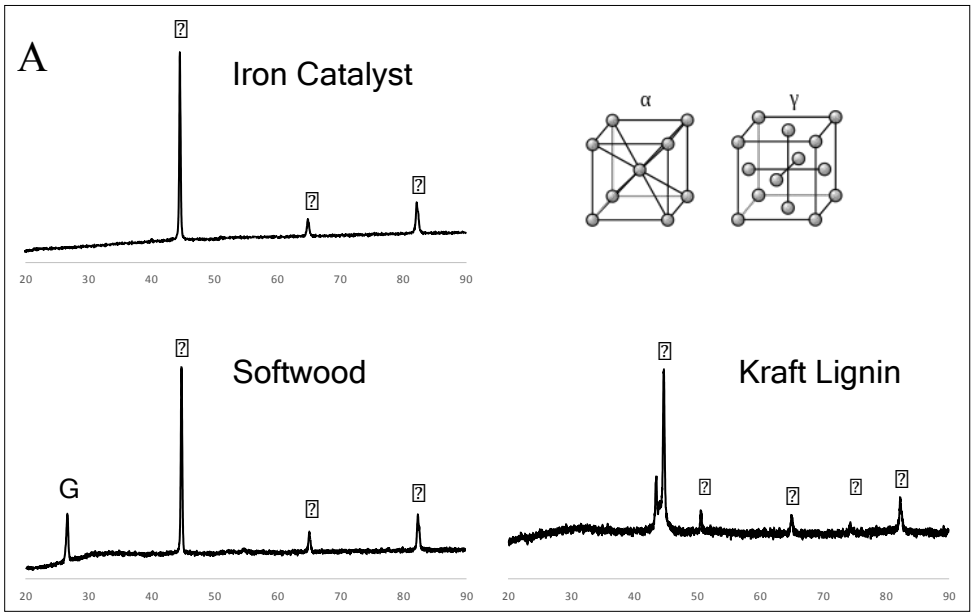

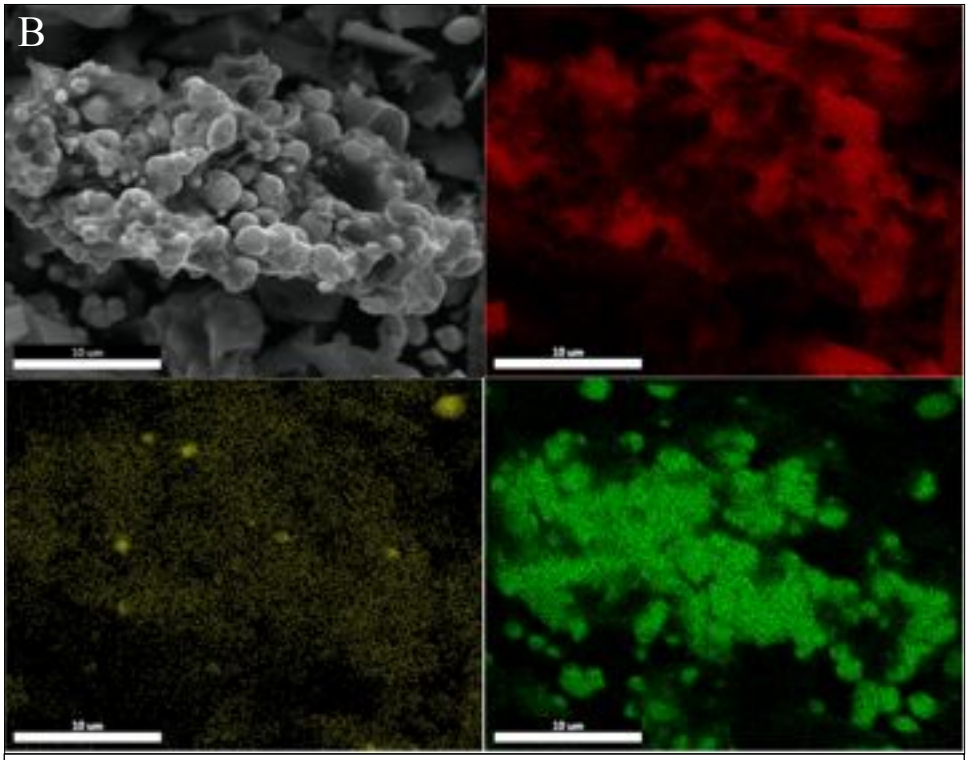

Figure 2. A) X-ray diffractograms of iron catalyst, softwood- and Kraft-lignin derived biographite materials (prior to iron removal) with peaks highlighted for graphite (G), the alpha allotrope of iron (α), and the gamma allotrope of iron (γ), with 2θ angles of diffraction listed on the x-axis. B) Energy-dispersive x-ray spectral mapping of Kraft lignin-derived biographite material (prior to iron removal). Red, yellow, and green represent carbon, sulfur, and iron, respectively.

Graphite crystallite size in the c-direction (Lc) and a-direction (La) are quantified for each biomaterial graphitized under baseline conditions, as shown in Figure 3A. Softwood produces graphite crystallites of the largest size in the a-direction and second largest size in the c-direction. Cellulose and glucose both produce graphite crystallites of relatively large size in the c-direction, but small size in the a-direction. Organosolv lignin and hydrolysis lignin produce graphite crystallites of relatively small size in the c-direction. Kraft lignin-derived materials are not included since Kraft lignin produces non-graphitic disordered carbon. Cross sectional areas are estimated by multiplying Lc and La, and degrees of graphitization are determined using Raman data and Equation S3, as shown in Figure 3B. Standard deviations in degree of graphitization are also shown in Figure 3B. The standard deviation in degree of graphitization provides an understanding of the uniformity of graphitic structure within the bulk material: low standard deviation (small circles) indicates high degree of uniformity, whereas high standard deviation (large circles) indicates a lesser degree of uniformity. Softwood generates graphite crystallites of the largest cross sectional areas and hydrolysis lignin generates a bulk material with the highest degree of graphitization. Interestingly, the biomaterials that melt to form a liquid intermediate phase during heating, namely the lignins and glucose, have smaller standard deviations and thus have relatively uniform distributions of graphitic structure relative to the non-melting biomaterials such as cellulose, softwood, and hardwood. Our simple method of graphitization involves dry mixing iron catalyst powder with solid biomaterial mass prior to thermal treatment, and thus the iron/biomaterial mixtures have spatial regions with little interaction between the iron and biomaterial. With melting biomaterials, the initial regions of little interaction are eliminated through diffusion of the iron catalyst in the liquid intermediate phase, whereas the non-melting biomaterials retain the regions of little interaction resulting in

voids of graphitic structure in the final product and a larger standard deviation in the degree of graphitization. Thus, certain regions in softwood are amenable to large crystal formation, whereas most regions in hydrolysis lignin are amenable to medium size crystal formation. The difference in trends observed indicates the process of graphitization is highly dependent on biomolecular structure, with the presence or absence of liquid intermediate phase being of particular importance. Hardwood and softwood biomaterials of two different particle sizes are assessed for graphite crystallite size and degree of graphitization, as shown in Figure 3C+D. Intuitively, large particles should react less with the iron catalyst than small particles, due to the decreased surface area of large particles. This intuition is confirmed for both softwood and hardwood, with the small particle size (150 – 425um) generating the largest crystallites in the c- and a-directions. In addition, the smallest particles generate biographite materials of the largest degree of graphitization. Notably, the increase in graphite quality from large to small particle size is much greater for softwood than for hardwood. Softwood of small particle size generates the highest quality graphite, nearly reaching that of commercial graphite. Glucose and softwood are graphitized using different heating methods to assess graphite crystal size and degree of graphitization, as shown in Figure 3E+F. The degree of graphitization for both glucose and softwood is highest with the longest heating method (hold). Glucose generates the largest crystallites with the fastest heating method, whereas softwood generates the largest crystallites with the baseline heating method. Overall, softwood generates larger graphite crystallites and a greater degree of graphitization than glucose. The difference in trends observed are complex and indicate that optimal heating method differs with biomolecular structure.

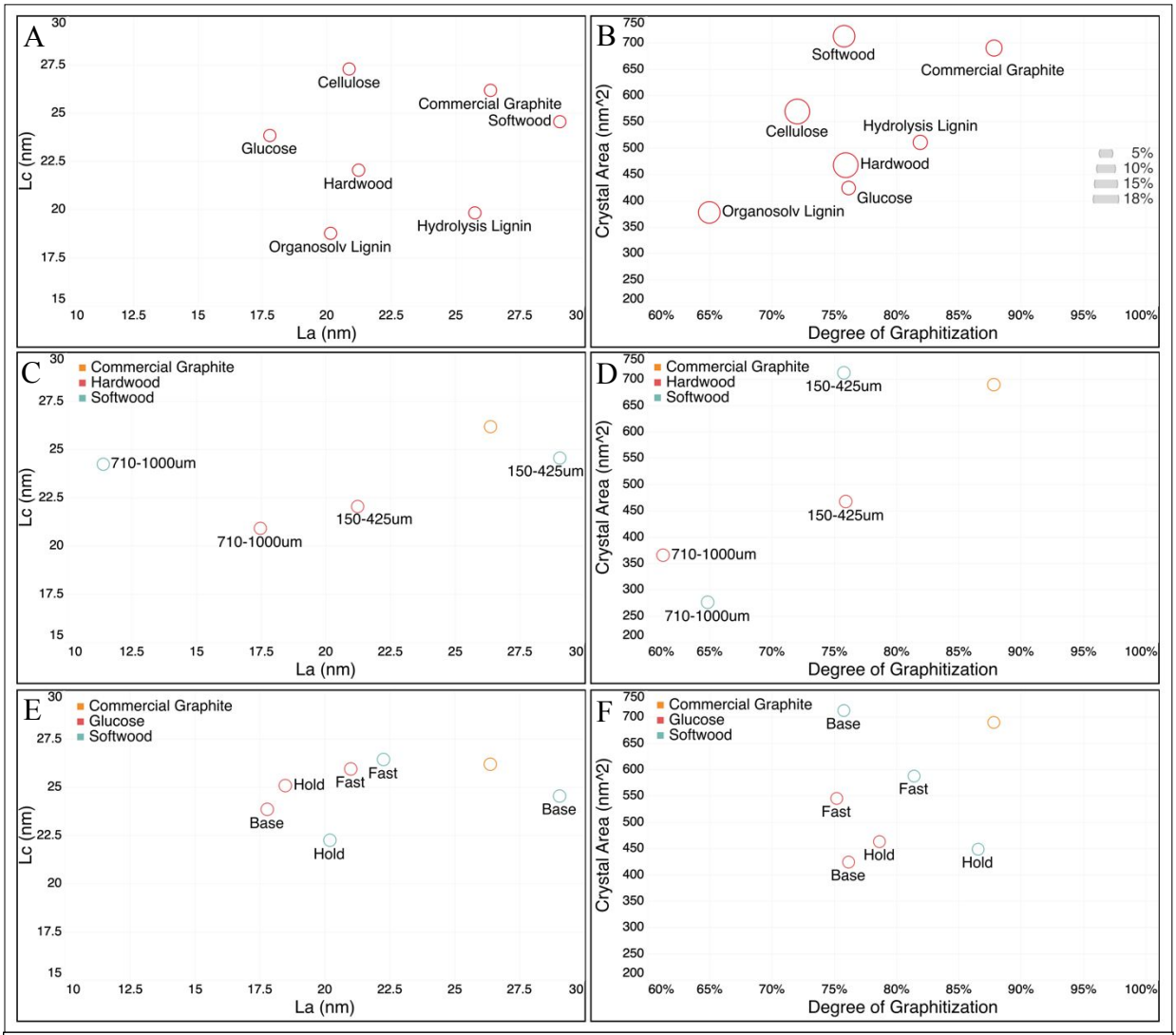

Figure 3. Graphite characterization of the various biographite materials produced using baseline conditions: A) graphite crystallite size in c-direction (Lc) vs. size in a-direction (La) and B) graphite crystallite area (nm^2) vs. degree of graphitization (standard deviation in degree of graphitization shown by circle size). Graphite characterization of softwood- and hardwood-derived biographite materials produced using different particle sizes: C) graphite crystallite size in c-direction (Lc) vs. size in a-direction (La) and D) graphite crystallite area (nm^2) vs. degree of graphitization. Graphite characterization of softwood- and glucose-derived biographite materials produced using different heating methods: E) graphite crystallite size in c-direction (Lc) vs. size in a-direction (La) and F) graphite crystallite area (nm^2) vs. degree of graphitization.

To refine our knowledge of the relationship between biomolecular structure and method of thermal treatment, we assess the graphitization of glucose and softwood at maximum temperatures of 600, 900, and 1200°C; the 1200°C thermal treatment is the baseline method of graphitization. As shown in Figure 4, the onset temperature for graphitization of glucose

(~600°C) is considerably lower than that for softwood (~900°C). This observation corroborates findings from the assessment of different heating methods (Figure 3E+F), wherein glucose graphitizes more quickly due to the lower onset temperature for graphitization, relative to softwood. Product yield is an important parameter with regards to the economic viability of any biomass conversion process. Overall, lignin provides the highest graphite yield and glucose the lowest yield, as shown in Figure S2. Thus, biomaterials high in oxygen content have the lowest biographite yields.

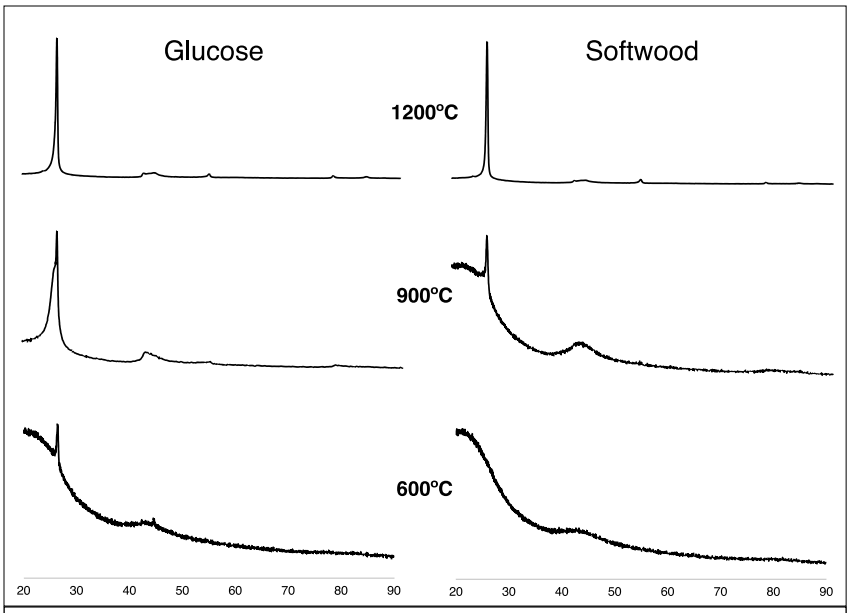

Figure 4. X-ray diffractograms of glucose- and softwood-derived biographite materials graphitized at different temperatures; 2θ angles of diffraction listed on x-axis.

Scanning electron microscopy is used to understand the morphologies of the various biomaterials treated in the study. Cellular structure morphology representative of woody biomass is detected in images of softwood treated at 600 and 1200°C, as shown in Figure 5A+B. Notably, graphitic platelet structure is detected through observation and comparison of biomaterials treated at different temperatures. Softwood and glucose treated at 600°C (Figure 8A+C) have

been proven to be nongraphitic, disordered carbon via XRD (Figure 4). In Figure 5A+C, indentations and thin shell casings where spherical iron particles were located prior to acid washing are evident, but there is an overall lack of observable evidence indicating high reactivity between the iron catalyst and biomaterial. However, Figure 5B+D shows evidence of flaky graphite platelets forming from reaction between the iron particles and biomaterial treated at 1200°C, with validation from XRD and Raman data (Figure 1). During heating, glucose melts and progresses through a liquid intermediate, which allows the iron catalyst particles to diffuse and distribute more uniformly, relative to softwood. However, iron catalyst does appear to distribute within the pores of the solid, non-melting softwood materials during graphitization (Figure 5B).

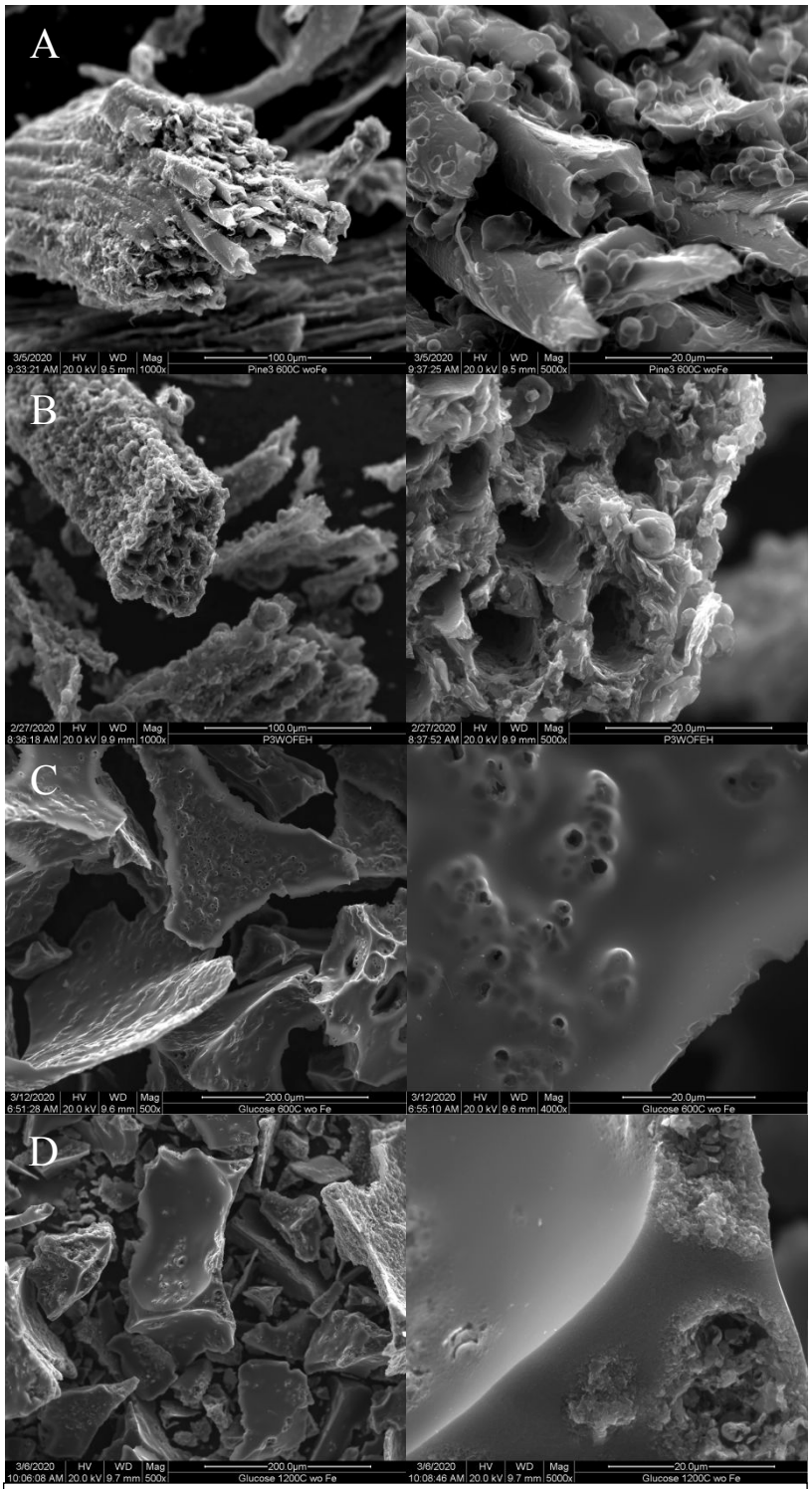

Figure 5. Scanning electron micrographs of biographite materials after iron removal via acid washing: A) softwood graphitized at 600°C, B) softwood graphitized at 1200°C, C) glucose graphitized at 600°C, and D) glucose graphitized at 1200°C

Evidence of graphite formation within softwood (Figure 5B) indicates that the iron particles melt and flow within the pores of the cellular matrix during heating, thereby distributing the iron catalyst within the biomass. Figure 6A shows an iron-carbon phase diagram, with the eutectic transition point at ~1150°C. At ~1150°C, the semi-molten iron becomes saturated in carbon and transitions to a full-molten liquid phase. Figure 6B shows a proposed mechanism of iron-catalyzed graphitization of softwood wherein 1) iron particle is resting on solid carbon (black circles) at temperature < 700°C, 2) temperature increases from 700 to 800°C, with iron particle beginning to transition from solid to liquid, 3) temperature increases from 800 to 900°C, with carbon beginning to solubilize in the semi-liquid iron particle, 4) temperature increases from 900 to 1000°C, with initial nucleation of graphite crystallites as the molten iron particle is partially saturated with carbon, 5) temperature increases from 1000 to 1200°C, with molten iron carbide fully saturated in carbon, 6) temperature remains constant at 1200°C, with molten iron carbide catalyzing the transformation of disordered carbon to graphitic carbon. At 1200°C, the activity of the iron catalyst reduces with time as graphitic carbon precipitation blocks access to disordered carbon.

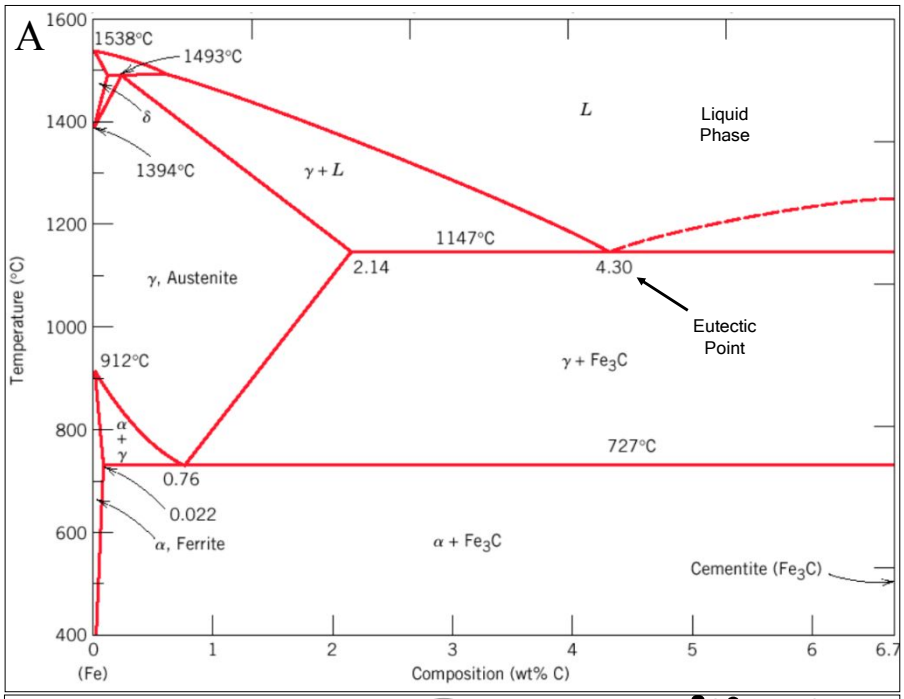

Figure 6. A) Iron-Iron Carbide (Fe-Fe_3C) phase diagram[41]. Catalytic graphitization occurs at the highest rate at temperatures between 1100-1200°C, wherein molten iron-carbide becomes saturated in carbon and precipitates graphite. B) Proposed mechanism of iron-catalyzed graphitization of softwood wherein iron melts (1-2) before solubilizing carbon to form molten iron carbide (3) which precipitates graphite upon reaching carbon saturation (4-6).

Further insight into the mechanisms involved in iron-catalyzed graphitization of biomaterials can be gained from past studies on graphite crystallization in cast iron. Stefanescu et al. (2018) hypothesized a three-stage mechanism of graphite formation during cast iron heating and cooling[40]: 1) crystallite nucleation in molten iron, 2) crystallite growth during eutectic iron-carbon formation, and 3) continued crystallite growth via graphite precipitation during cool

down as molten iron solidifies and the solubility of carbon decreases. The bulk of graphite crystallite growth takes place at temperatures in the range of 1100 – 1200°C, or the eutectic point at which iron carbide transitions from solid to liquid.[41] Generally, graphite grows from molten iron carbide in the form of platelets, which we have observed in our work (Figures 7A & 8D-F), but the final morphologies of the aggregated platelets vary depending on local composition and degrees of supersaturation and undercooling; the biographite platelets appear similar in structure to those in the commercial synthetic graphite product, as shown in Figure S3. Our work has identified three primary morphological transformations during catalytic graphitization of biomaterials, which agree with graphite morphologies identified in cast iron production: 1) nucleation followed by curved growth of graphite crystallites forming spheroids (Figure 7B), 2) nucleation followed by foliated growth of graphitic crystallites forming layered sheets of graphite (Figure 7C), and 3) nucleation followed by spiral growth of graphite crystallites forming disoriented platelets (Figure 7D). Notably, the graphitization mechanism primarily progresses through liquid-solid interactions, with the molten liquid iron interacting with solid carbon and inducing crystallite growth.

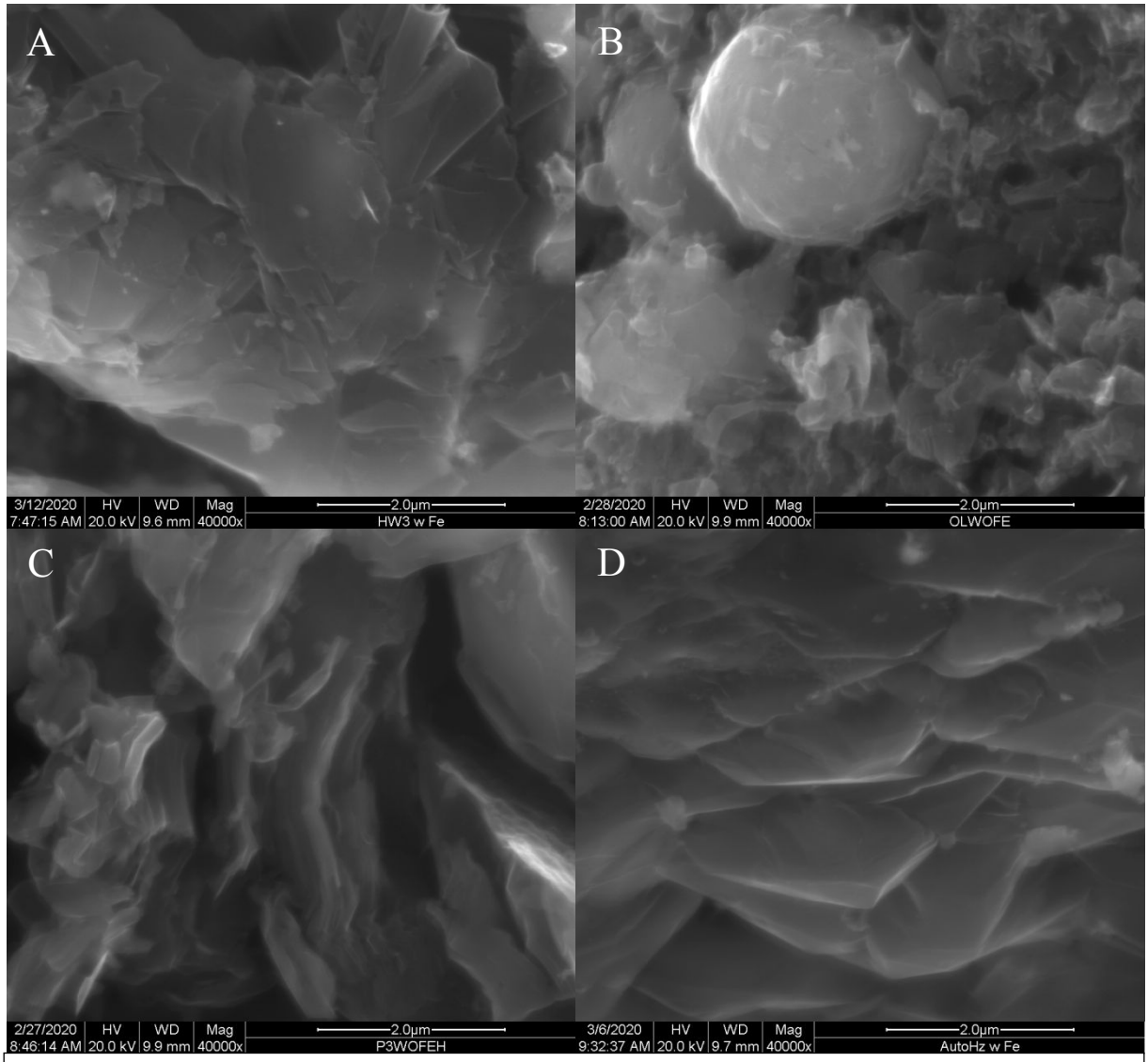

Figure 7. Scanning electron micrographs of A) graphite platelets grown from the iron catalyst during biomass graphitization, B) aggregated graphite platelets forming a spheroid, C) aggregated graphite platelets forming foliated layering, and D) aggregated graphite platelets forming a disoriented spiral pattern.

To understand the biographite morphology at a smaller scale, we conduct transmission electron microscopy (TEM). As shown in Figure 8A-C, TEM images show graphitic carbon shells that precipitate from iron particles during graphitization, corroborating the proposed mechanism in Figure 6. As shown in Figure 8B, the stacking of graphitic sheets in the c-direction (Lc) is ~20 – 30nm, which corroborates the average Lc value determined via XRD, shown in Figure 3A. As shown in Figure 8C, small iron particles appear to have the ability to generate

multiple graphitic shells through dynamic graphitization wherein the shells grow and separate from the iron particle; also, TEM data show iron particles of very small size (< 50nm), which likely originate from larger iron particles (> 1um) and form after melting and resolidification. As shown in Figure 8D-F, ordered graphitic platelets grown from larger iron particles are observed.

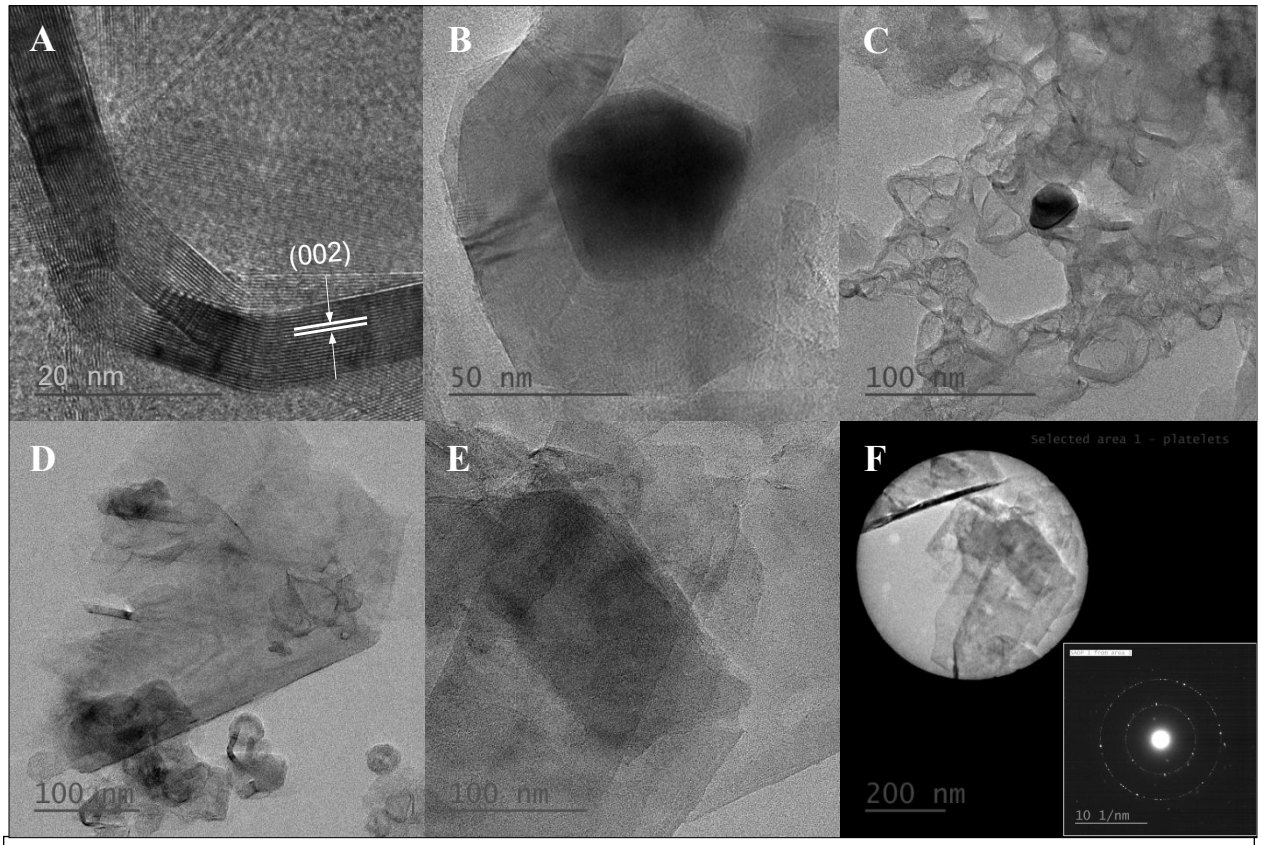

Figure 8. Transmission electron micrographs of softwood-derived graphitic carbon formation via iron catalysis at 1200°C A) graphitic sheets with interlayer (002) d-spacing, B-C) graphite precipitation from iron particle, and D-F) ordered graphitic platelets (with the selected-area electron diffraction (SAED) pattern in panel F).

To further elucidate the mechanism of graphitization and better understand the role of biomolecular configuration, we assess a multitude of additional biomaterials via scanning electron microscopy, as shown in Figure 9. The cellular structure morphology representative of woody biomass is evident in the cross sectional image shown in Figure 9A, wherein the depth of catalyst penetration is revealed. Iron catalyst on the exterior of the hardwood fibers appears to

catalyze graphitization of carbon several micrometers deep into the fiber walls. Interestingly, the depth of catalyst penetration is greater for softwood than for hardwood, corroborated by morphological micrographs shown in Figures 5B and 9A. Hardwood cellular structure is more complex than softwood due to the large number of cell types and the variability among cell types, which likely inhibits molten catalyst transport in hardwood cells and thus results in less graphitization.[31] Figures 9B, C, and D show micrographs of graphitized lignins, all of which form intermediate liquid phases during initial heating and result in a solidified material that resembles shattered glass upon crushing via mortar and pestle. Graphitic platelets are clearly observed in the materials derived from organosolv and hydrolysis lignins, as shown in Figures 9B and C. The morphology of carbonized Kraft lignin (Figure 9D) shows no evidence of graphitic structure and appears similar to that of glucose carbonized at 600°C (Figure 5C) both of which have been proven to be constructed of nongraphitic, disordered carbon (Figures 1 & 4).

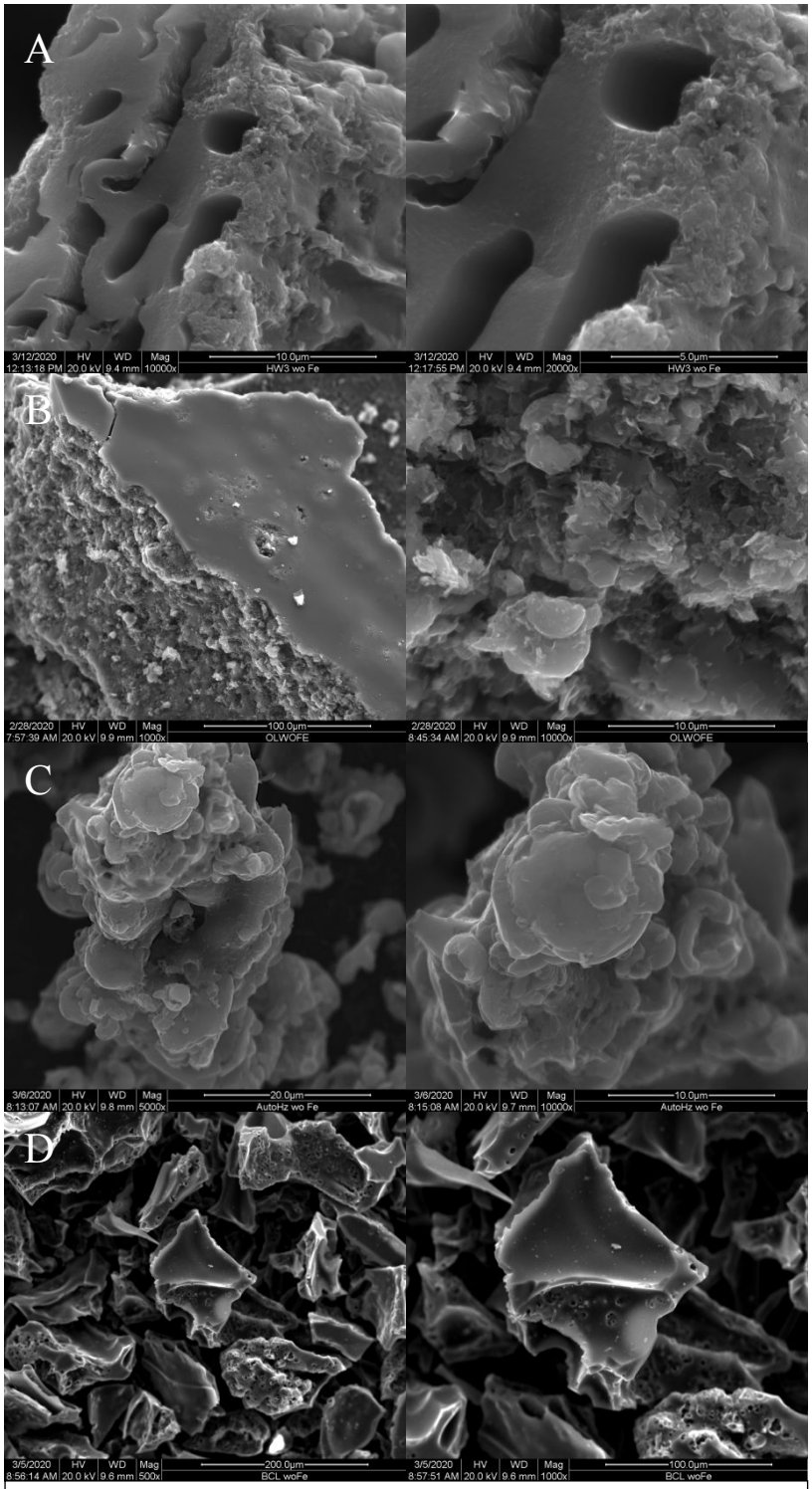

Figure 9. Scanning electron micrographs of biographite materials produced under baseline conditions with iron removal: A) hardwood, B) organosolv lignin, C) autohydrolysis lignin, and D) Kraft lignin.

Energy-dispersive x-ray spectral (EDS) mapping is used to understand the morphology and distribution of iron and carbon in graphitized materials prior to acid washing, as shown in Figure 10. The detection of iron and carbon is confined to several micrometers within the surface of the materials analyzed, and thus EDS does not provide insight into the composition of the inner mass within large particles. As shown in Figures 10A and B, the distribution of iron and carbon in graphitized softwood appears to be more uniform than that in hydrolysis lignin. According to XRD and Raman data (Figure 3A+B), softwood-derived biographite is of larger crystallite size but smaller degree of graphitization compared with hydrolysis lignin. Therefore, large graphite crystallites are highly concentrated near the surface of softwood particles, with disordered regions concentrated within the core of the particles where iron catalyst has difficulty reaching. Hydrolysis lignin forms a liquid intermediate phase during heating which forms relatively small particles during graphitization, with iron distributed more uniformly within the core of the particles, relative to softwood. As shown in Figure 10B, iron and hydrolysis lignin-derived biographite are agglomerated together, indicating intimate contact during graphitization. As shown in the high magnification micrographs in Figure 10A+B, the irregular morphology of the iron indicates the initial spherical iron particles melt, react with carbon, precipitate graphite, and then solidify during cool down, thereby supporting the proposed mechanism of graphitization shown in Figure 6B. As shown in Figure 10C, the spherical iron catalyst particles in Kraft lignin retain their initial shape and morphology throughout heating and never melt. The lack of iron phase change indicates iron never reaches the eutectic transition point in Kraft lignin and thus never precipitates graphite platelets. The reason for the reduced reactivity of iron in Kraft lignin appears to be partly due to the presence of sulfur and the gamma allotrope (Figure

2), both of which prevent the iron from transitioning phases and catalyzing the production of graphite platelets.

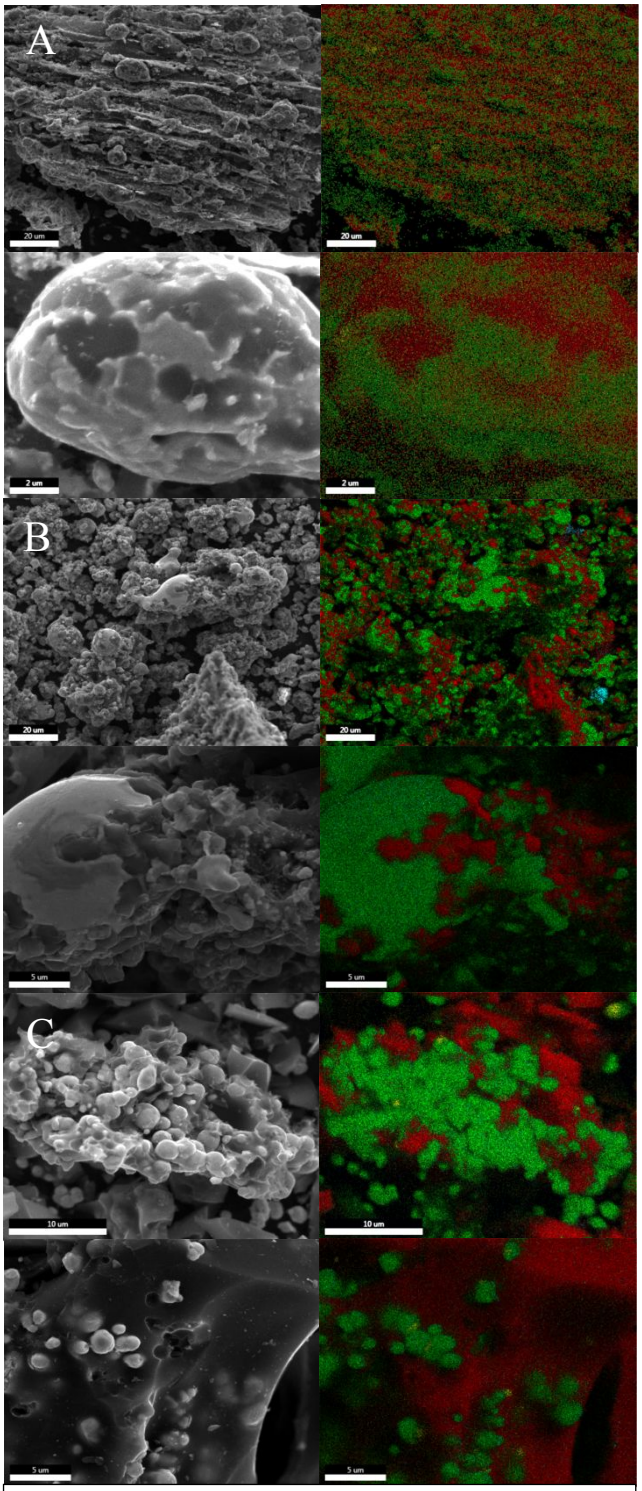

Figure 10. Scanning electron micrographs and corresponding energy-dispersive x-ray spectral mapping of biographite materials produced using the baseline procedure without iron removal. Green and red represent presence of iron and carbon, respectively. A) softwood, B) hydrolysis lignin, and C) Kraft lignin.

The main motivation behind this study is to develop a simple, scalable, and relatively green alternative to the current graphite anode material used in lithium-ion batteries, and the only way to ensure new graphite materials are adequate for battery application is to test electrochemical performance. Softwood-derived biographite is selected for electrochemical performance in a coin-type half-cell. The BET surface area of softwood-derived biographite is 25.99 m^2/g, which is slightly higher than that of commercial graphite (5 - 20 m^2/g).[42] The anode volume used for electrochemical testing is relatively high, and densification should be explored in future work. The inorganic content of the clean pine (softwood) used for graphitization is 0.7 wt%, and that of the carbonized pine is 1.7 wt% (not including Fe), as determined in our prior work that used the same pine feedstock.[43] The hydrochloric acid effectively removes the iron catalyst and other inorganics, as shown in Figure S4; note that silicon is not detected of any appreciable quantity in the pine biographite product. Figure 11A represents the galvanostatic discharge and charge profiles of the biographite tested at 0.1C in the voltage window of 0.005-1.5 V. During the first cycle, the characteristic voltage plateaus due to the staging mechanism are observed with discharge and charge capacities of 399.08 and 335.09 $mAhg^{-1}$, respectively. The calculated initial Coulombic efficiency (CE) is 83.96%, and most capacity loss is attributed to the reduction of electrolyte and the formation of a stable solid-electrolyte interphase (SEI) layer.[44,45] The electrochemical reactions related to the SEI formation are inferred by sloping voltage profile from 0.8 to 0.3 V. Irreversibility of the SEI formation is well supported by the disappearance of the cathodic peaks originated from SEI formation reactions in subsequent cycles (Figure 11B). CE of the second cycle is drastically increased up to 98.08% based on discharge and charge capacities of 344.33 and 335.09 $mAhg^{-1}$, respectively.

To understand the detailed storage mechanism of Li^+ ions—intercalation and de-intercalation with biographite—the differential capacity (dQ/dV) of the 1st and 2nd discharge and charge cycles are analyzed, as shown in Figure 11B. During initial Li^+ ion intercalation (discharge), the cathodic peaks at around 0.74 and 0.67 V (*vs* Li/Li^+, hereafter) are shown in the green color-highlighted inset. These initial peaks are observed during the first cycle and are attributed to the irreversible SEI formation as discussed above. Below 0.3 V, three additional cathodic peaks are observed at around 0.20 (blue color-highlighted inset), 0.11 and 0.07 V, respectively. These peaks originate from the Li^+ ion staging mechanisms, including phase transitions that are dependent on the content of intercalated Li^+ ions.[46,47] Specifically, three cathodic peaks correspond to the following phase transitions: 1) diluted stage I to stage IV, 2) stage IV to stage II and III, and 3) stage II to stage I. During the subsequent Li^+ ion de-intercalation (charge), three anodic peaks from the reverse staging processes are observed, which demonstrate the electrochemical reversibility of the biographite. During the second cycle, the dQ/dV peaks relate to staging mechanisms and shift to relatively high voltages, with electrochemical reactions occurring readily at lower overpotentials mainly due to the formation of stable SEI with high Li^+ ion transport property.

The rate capability of the biographite is tested to understand the reversible Li^+ ion intercalation and de-intercalation behaviors at high C-rate, as shown in Figure 11C. The specific reversible capacities of approximately 340, 300, 245, 120, 40 and 15 $mAhg^{-1}$ are observed at 0.1C, 0.5C, 1C, 2C, 4C and 8C, respectively. The detailed discharge and charge profiles with varying C-rate are shown in Figure 11D. The biographite shows large capacity reduction with high C-rate, but demonstrates outstanding capacity self-recovery. In addition, galvanostatic long-term cycling test (at 0.5C) is performed to evaluate the cyclability of the biographite material, as

shown in Figure 11E and F. Two formation cycles (0.1C) prior to faster cycling (0.5C) are incorporated to form the stable SEI layer and activate the electrode. The capacity retention is 89% at 100 cycles with > 99% of Coulombic efficiency. These results conclude that the well-synthesized biographite has a great potential as an anode material for lithium-ion batteries compared with previously reported results (Table S1).

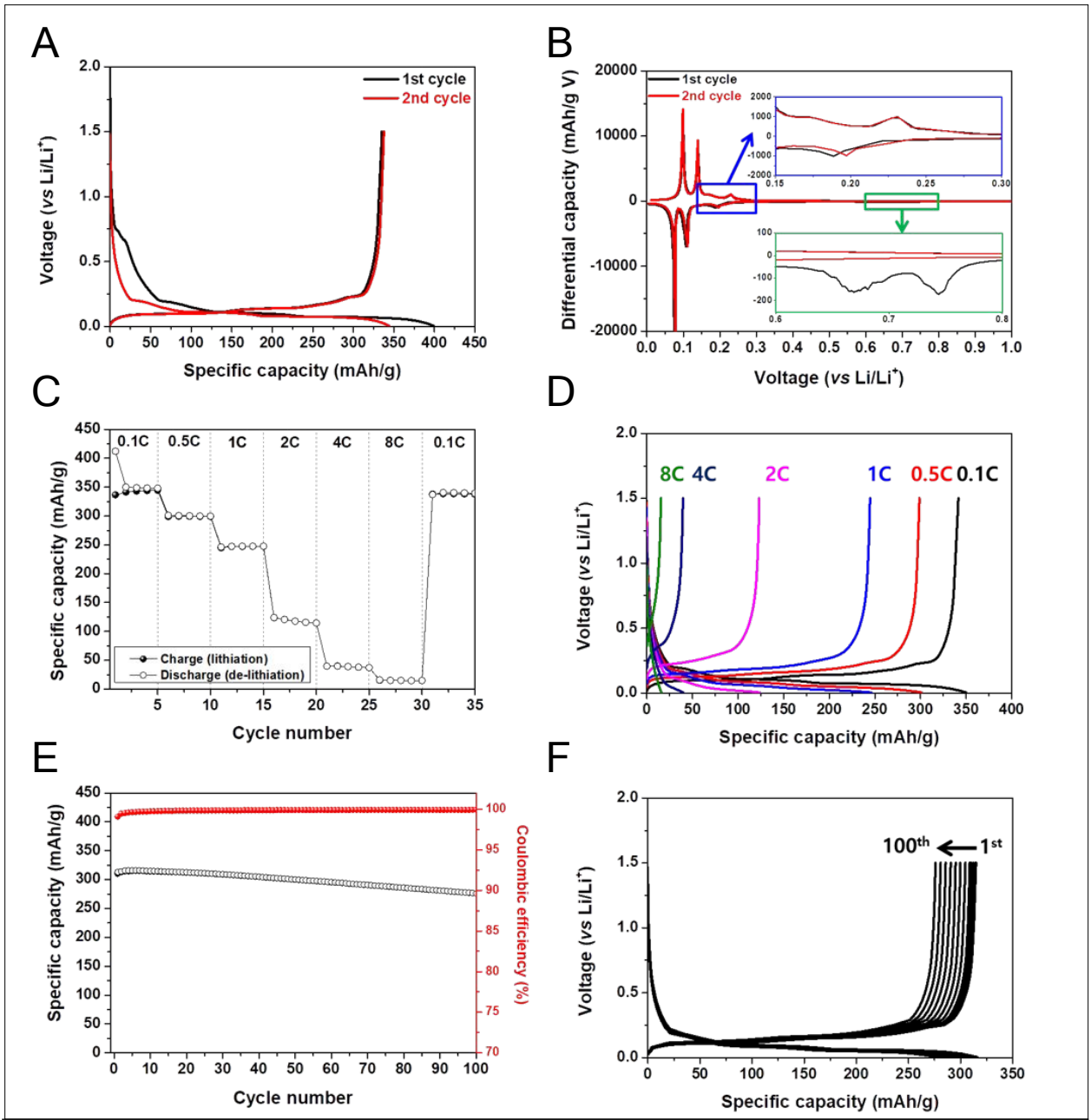

Figure 11. Electrochemical performance of softwood biographite: A) galvanostatic discharge and charge profiles and B) differential capacity (dQ/dV) plots at 0.1C in the voltage window of 0.005-1.5 V for the 1st and 2nd cycles. C) rate capability plot and D) corresponding galvanostatic discharge and charge profiles at varying C-rates from 0.1C to 8C. E) cycling stability plot and F) corresponding galvanostatic discharge and charge profiles at 0.5C over 100 cycles.

Conclusions

For the first time, a multitude of biomaterials, including softwood, hardwood, cellulose, glucose, organosolv lignin, and hydrolysis lignin, are successfully converted to high quality graphite using a simple and scalable iron-catalyzed process. Biomass particle size and method of heating are varied to understand their effects on graphitization. Biographite materials are characterized and compared based on graphite mass yield, graphite crystallite size, degree of graphitization, graphite uniformity, iron catalyst distribution, and graphite crystallite morphology. The onset temperature of graphitization is lower for glucose (~600°C) than for lignocellulose (~900°C), and optimal heating rates vary with biomolecular structure. Small biomaterial particles result in better quality graphite, relative to large particles, due to increased surface area and more reactivity between biomaterial and catalyst. Graphite mass yield is highest for biomaterials with low oxygen content, such as lignin, and lowest for biomaterials with high oxygen content, such as glucose. Softwood generates the largest graphite crystallites and hydrolysis lignin generates a bulk material with the highest degree of graphitization. Biomaterials that melt to form a liquid intermediate phase during heat ramp, such as glucose and lignin, have higher graphite uniformity than those without melting points, such as lignocellulose. Future research should involve advanced analytical techniques such as in-situ x-ray diffraction and molecular-beam mass spectrometry to elucidate intermediate phase chemistry involved in the molecular transformation of the various biomaterials. At the eutectic transition point (~1100 – 1200°C), molten iron-iron carbide complexes catalyze the conversion of disordered, amorphous carbon to graphite in the form of aggregated platelets. Graphite platelets aggregate to form three primary morphologies: spheroids, foliated layers, and disoriented spiraling patterns. Of the seven biomaterials assessed, Kraft lignin is the only material incapable of graphitization

due to inadequate phase transition of the iron catalyst. Further research is warranted to understand the inherent limitations of Kraft lignin graphitization, including the use of treatment temperatures higher than 1200°C. In addition, the procedure should be optimized to determine the minimum effective catalyst loading. Softwood-derived biographite demonstrates excellent electrochemical performance in a lithium-ion coin cell with capacity retention of 89% over 100 cycles and > 99% Coulombic efficiency. Future research should be conducted to understand the effect residual inorganics have on electrochemical performance. This study demonstrates the great potential of biographite as a relatively green anode material for lithium-ion batteries.

Conflicts of Interest

There are no conflicts to declare.

Acknowledgements

We would like to acknowledge Dr. Steve Kelley for his advice on experimental design, Eliezer Reyes Molina for quantifying BET surface area, Lisa Lentz at NCSU's Environmental & Agricultural Testing Service (EATS) laboratory for conducting elemental analysis, and Christopher Winkler at NCSU's Analytical Instrumentation Facility (AIF) for taking high resolution images of the biographite materials via transmission electron microscopy (TEM). This work was supported, in part, by a US Office of Science Graduate Student Research (SCGSR) Fellowship granted to William J. Sagues. This work was supported, in part, by the USDA-NIFA project (award number 2017-67009-26771, program code A6131), Preparing Diverse and Rural Students and Teachers to Meet the Challenges in the Bioproducts and Bioenergy Industry. This work was supported, in part, by the Laboratory Directed Research and Development (LDRD) program at National Renewable Energy Laboratory (NREL).

Author Contributions

W.J.S. and S.P. conceived the study; W.J.S. and N.M. conducted the biomaterial graphitization and purification experiments; W.J.S. and T.V. conducted the scanning electron microscopy and energy dispersive x-ray spectral mapping; W.J.S. and M.Y. conducted the x-ray diffraction and Raman spectroscopy; W.J.S., J.Y., and S.-D.H. conducted the electrochemical tests. W.J.S. analyzed data and wrote the paper with input from all coauthors.

References

1 H. Pierson, *Handbook of carbon, graphite, diamond and fullerenes*, Noyes Publications, 1993.

2 E. A. Olivetti, G. Ceder, G. G. Gaustad and X. Fu, *Joule*, 2017, **1**, 229–243.

3 S. Moores, *Benchmark Miner. Intell.*, 2019.

4 M. Burton and E. Van Der Walt, Electric-Car Revolution Shakes Up the Biggest Metals Markets, https://www.bloomberg.com/news/articles/2017-08-02/electric-car-revolution-is-shaking-up-the-biggest-metals-markets.

5 A. Mayyas, Are there enough materials to cover li- ion batteries?, https://www.jisea.org/20180815.html.

6 D. Bogdanov, J. Farfan, K. Sadovskaia, A. Aghahosseini, M. Child, A. Gulagi, A. S. Oyewo, L. de Souza Noel Simas Barbosa and C. Breyer, *Nat. Commun.*, 2019, **10**, 1–16.

7 G. Crabtree, *Science (80-.).*, 2019, **366**, 422–424.

8 J. B. Dunn, L. Gaines, M. Barnes, J. Sullivan and M. Wang, Material and Energy Flows in the Materials Production, Assembly, and End-of-Life Stages of the Automotive Lithium-Ion Battery Life Cycle, http://www.osti.gov/bridge.

9 J. Whiteside and D. Finn-Foley, Supply Chain Looms as Serious Threat to Batteries' Green Reputation, https://www.greentechmedia.com/articles/read/graphite-the-biggest-

threat-to-batteries-green-reputation.

10 National Enviromental Research Council, Risk List 2015 - An update to the supply risk index for elements or element groups that are of economic value, https://www.bgs.ac.uk/mineralsuk/statistics/riskList.html.

11 US Department of the Interior - Office of the Secretary: Final List of Critical Minerals 2018, https://www.govinfo.gov/content/pkg/FR-2018-05-18/pdf/2018-10667.pdf.

12 J. Li, C. Daniel and D. Wood, *J. Power Sources*, 2011, **196**, 2452–2460.

13 N. Lebedeva, F. Persio and L. Boon-Brett, Lithium ion battery value chain and related opportunities for Europe, https://ec.europa.eu/jrc/sites/jrcsh/files/jrc105010_161214_li-ion_battery_value_chain_jrc105010.pdf.

14 A. D. Jara, A. Betemariam, G. Woldetinsae and J. Y. Kim, *Int. J. Min. Sci. Technol.*, 2019, **29**, 671–689.

15 A. N. Sawarkar, A. B. Pandit, S. D. Samant and J. B. Joshi, *Can. J. Chem. Eng.*, 2007, **85**, 1–24.

16 S. Schimmelpfennig and B. Glaser, *J. Environ. Qual.*, 2012, **41**, 1001–1013.

17 M. Romare and L. Dahllöf, The Life Cycle Energy Consumption and Greenhouse Gas Emissions from Lithium-Ion Batteries, http://www.ivl.se/download/18.5922281715bdaebede9559/1496046218976/C243+The+life+cycle+energy+consumption+and+CO2+emissions+from+lithium+ion+batteries+.pdf.

18 J. S. McDonald-Wharry, M. Manley-Harris and K. L. Pickering, *Energy and Fuels*, 2016, **30**, 7811–7826.

19 R. E. Franklin, *Proc. R. Soc.*, 1951, **209**, 196–218.

20 K. Xu, Y. Li, J. Xiong, X. Ou, W. Su, G. Zhong and C. Yang, *Front. Chem.*, 2018, **6**, 1–

10.

21 H. H. Nguyen, N. V. To, T. V. Tran, K. V. Nguyen, S. T. Luong, N. N. T. Nguyen, C. V. Hoang, H. S. Nguyen and N. V. Nguyen, *Appl. Phys. A Mater. Sci. Process.*, , DOI:10.1007/s00339-020-03713-0.

22 Y. Li, Y. S. Hu, H. Li, L. Chen and X. Huang, *J. Mater. Chem. A*, 2015, **4**, 96–104.

23 J. R. Dahn, T. Zheng, Y. Liu and J. S. Xue, *Science (80-.).*, 1995, **270**, 590–594.

24 W. J. Sagues, A. Jain, D. Brown, S. Aggarwal, A. Suarez, M. Kollman, S. Park and D. S. Argyropoulos, *Green Chem.*, 2019, **21**, 4253–4265.

25 Q. Hu, Q. Mao, X. Ren, H. Yang and H. Chen, *Bioresour. Technol.*, 2019, **275**, 53–60.

26 N. A. Banek, D. T. Abele, K. R. McKenzie and M. J. Wagner, *ACS Sustain. Chem. Eng.*, 2018, **6**, 13199–13207.

27 A. Gomez-Martin, J. Martinez-Fernandez, M. Ruttert, A. Heckmann, M. Winter, T. Placke and J. Ramirez-Rico, *ChemSusChem*, 2018, **11**, 2776–2787.

28 E. Thompson, A. E. Danks, L. Bourgeois and Z. Schnepp, *Green Chem.*, 2015, **17**, 551–556.

29 L. Zhao, J. C. Bennett and M. N. Obrovac, *Carbon N. Y.*, 2018, **134**, 507–518.

30 L. Zhao, X. Zhao, L. T. Burke, J. C. Bennett, R. A. Dunlap and M. N. Obrovac, *ChemSusChem*, 2017, **10**, 3409–3418.

31 A. C. Wiedenhoeft, *Structure and function of wood. Wood handbook: Wood as an engineering material: Chapter 3. General technical report FPL GTR-190*, 2010.

32 Asbury Carbons - Synthetic graphite, https://asbury.com/materials/graphite/.

33 H. L. Zhang, F. Li, C. Liu and H. M. Cheng, *J. Phys. Chem. C*, 2008, **112**, 7767–7772.

34 S. Komaba, M. Watanabe, H. Groult and N. Kumagai, *Carbon N. Y.*, 2008, **46**, 1184–

1193.

35 S. Yoon, H. Kim and S. M. Oh, *J. Power Sources*, 2001, **94**, 68–73.

36 M. S. Park, J. Lee, J. W. Lee, K. J. Kim, Y. N. Jo, S. G. Woo and Y. J. Kim, *Carbon N. Y.*, 2013, **62**, 278–287.

37 S. Tachibana, *NUCLEATION AND GROWTH OF IRON SULFIDE ON METALLIC IRON PARTICLES UNDER LOW- PRESSURE PROTOPLANETARY DISK CONDITIONS*, 2012.

38 Y. H. Chen, Y. H. Chen, W. D. Hsu, Y. C. Chang, H. S. Sheu, J. J. Lee and S. K. Lin, *Sci. Rep.*, 2019, **9**, 1–6.

39 Iron and sulfur reaction, https://edu.rsc.org/experiments/iron-and-sulfur-reaction/713.article.

40 D. M. Ştefănescu, G. Alonso, P. Larrañaga, E. de La Fuente and R. Suárez, *Mater. Sci. Forum*, 2018, **925**, 36–44.

41 W. Callister Jr and D. Rethwisch, *Callister's Materials Science & Engineering 8th Ed.*, 2009.

42 M. Winter, P. Novak and A. Monnier, *Graphites for Lithium-Ion Cells: The Correlation of the First-Cycle Charge Loss with the Brunauer-Emmett-Teller Surface Area*, 1998, vol. 145.

43 S. Yoo, S. S. Kelley, D. C. Tilotta and S. Park, *ACS Sustain. Chem. Eng.*, 2018, **6**, 2621–2629.

44 J. S. Gnanaraj, R. W. Thompson, S. N. Iaconatti, J. F. Dicarlo and K. M. Abraham, *Electrochem. Solid-State Lett.*, 2005, **8**, A128–A132.

45 D. Aurbach, B. Markovsky, I. Weissman, E. Levi and Y. Ein-Eli, *Electrochim. Acta*,

1999, **45**, 67–86.

46 M. D. Levi and D. Aurbach, *J. Electroanal. Chem.*, 1997, **421**, 79–88.

47 D. Aurbach, *J. Electrochem. Soc.*, 1995, **142**, 2882.